Materials Advances

ROYAL SOCIETY OF CHEMISTRY

PAPER

View Article Online
View Journal | View Issue

Check for updates

Cite this: *Mater. Adv.*, 2024, 5, 9641

Disorder induced augmentation of the specific capacitance of δ-MnO_2 nanoflowers by incorporating Fe_3O_4 nanodiamonds for supercapacitor electrodes†

Md. Raihan Siddiki,[a] Shahid Abubakar Abtahee,[ac] Mizanur Rahaman,[b] Muhammad Rakibul Islam[b] and Md. Abdullah Zubair*[a]

Received 3rd September 2024,
Accepted 7th November 2024

DOI: 10.1039/d4ma00880d

rsc.li/materials-advances

In this study, delta manganese dioxide (δ-MnO_2) nanoflowers and magnetite (Fe_3O_4) nanodiamond incorporated δ-MnO_2 nanoflowers (δ-MnO_2/Fe_3O_4 nanocomposites) were synthesized *via* a simple hydrothermal method for electrode materials in supercapacitors. The Fe_3O_4 content was varied between 0 and 5 wt% to determine the optimized combination of δ-MnO_2 and Fe_3O_4 for the nanocomposite that would exhibit superior electrochemical properties for high-performance energy storage devices. In a three-electrode system, the δ-MnO_2/Fe_3O_4 nanocomposite with 3 wt% Fe_3O_4 exhibited the highest specific capacitance of 459 F g^{-1} at a current density of 0.3 A g^{-1}, compared to 76 F g^{-1} for pure δ-MnO_2 nanoflowers and retained about 75% of its initial capacitance after 4000 charge–discharge cycles at a high current density of 6 A g^{-1}. The modulation of the electrochemical performance of the nanostructured composites was evaluated in terms of crystallographic and morphological aspects like interplanar spacing, crystallinity, defect formation and internal surface modification of the nanostructures and electrochemical impedance spectroscopic analysis. This study demonstrates that the optimized δ-MnO_2/(3%) Fe_3O_4 nanocomposite, with its high charge storage capacity and good long-term stability, is a relatively more effective electrode material for high-performance supercapacitors compared to other combinations with different morphologies.

Introduction

Recently, nanostructured metal oxides with transitional properties are considered as favorable options for extensive research for developing energy storage device-electrodes due to their compositional diversities, morphologies, large specific surface area, and high specific capacitance. They play a crucial role in making electrochemical supercapacitors, offering improved capacitance through defects and surface/interface control at the nanoscale. Despite their appreciable characteristics, challenges associated with low electrical conductivity, uncontrollable volume expansion, and slow ion diffusion prevent the metal oxides from reaching their peak potential.[1–10] Nevertheless, numerous efforts, including doping, multi-cation formation, introducing porous structures, and compositing, have been made to assist these promising compounds to surpass their constraints, enabling them to thrive and contribute to the optimization sought by researchers.[11–20]

Among the rigorously researched metal oxides for supercapacitor electrodes, MnO_2 has garnered significant interest due to its advantages, including natural abundance, low work function (4.4 eV), reversible charge–discharge characteristics, cost-effectiveness, and high specific theoretical capacitance (1370 F g^{-1}).[21–26] Several studies have focused on various morphologies of MnO_2 nanoparticles, particularly in the context of composite materials.[27–35] A favorable component for combining with MnO_2 or Mn_2O_3 is Fe_3O_4 (magnetite), owing to its outstanding magnetic and surface properties. The presence of different valence states in Fe_3O_4 enhances electrical conductivity, arising from electron transitions between Fe^{2+} and Fe^{3+} cations in the octahedral sites. Typically, composites incorporating Fe_3O_4 exhibit stability and recyclability; on top of that surface functionalization further contributes to the stability and increased specific surface area of Fe_3O_4 nanoparticles.[36,37]

[a] Department of Nanomaterials and Ceramic Engineering, Bangladesh University of Engineering and Technology, Dhaka, Bangladesh.
E-mail: mazubair2017@gmail.com
[b] Department of Physics, Bangladesh University of Engineering and Technology, Dhaka, Bangladesh
[c] Mechanical Engineering and Engineering Science, The University of North Carolina at Charlotte, North Carolina, USA

† Electronic supplementary information (ESI) available. See DOI: https://doi.org/10.1039/d4ma00880d

Iron oxide materials also have limitations when used alone, due to their inherently low electrical conductivity and slow ion diffusion kinetics. Numerous iron oxide-based electrodes with varying nanostructures were tried, such as spheres, buttons, microspheres, octahedra, nanowires, *etc.*, and they have demonstrated convincing electrochemical performance. Similar to other nanocomposites, in order to eliminate their individual shortcomings, iron oxides, especially Fe_3O_4, have been combined with MnO_2 for electrochemical applications.[38–43] Their combinations were reported to be successful in boosting electrochemical properties. For instance, Zeng and colleagues developed a low-temperature technique for assembling MnO_2 nanosheets over Fe_2O_3 nano-spindles, resulting in improved capacity retention.[44] Zhu *et al.* also achieved a high specific capacitance of 448 F g^{-1} at 5 mV s^{-1} using MnO_2 microspheres incorporated with Fe_3O_4 nanoparticles.[45] Besides, Sarkar *et al.* fabricated Fe_2O_3@MnO_2 core@shell nanowire heterostructures with superior supercapacitor performance compared to bare Fe_2O_3 nanowires.[46] Tu *et al.* synthesized a MnO_2@Fe_3O_4 double hollow nanosphere and formed an asymmetric supercapacitor with activated carbon (AC). It exhibited a specific capacitance of 375.14 F g^{-1} at 0.5 A g^{-1}.[38] Chen *et al.* produced Yolk@shell structured Fe_3O_4@MnO_2 microspheres, which displayed a capacitance of 715 F g^{-1} at 1 A g^{-1}. Integrating MnO_2 and iron oxide in one structure shows great potential for creating high-performance supercapacitor electrodes. This combination may offer advantages such as increased specific capacitance due to the high redox electroactivity of both materials and a shortened diffusion path, promoting fast and reversible faradaic reactions.[47]

In this work, diamond shaped Fe_3O_4 nanoparticles were integrated into birnessite (δ)-MnO_2 as a means to enhance the specific capacitance of the latter. δ-MnO_2 particles had flower shaped nanostructures, and they were grown with a hierarchical configuration of numerous nano-petals. To the best of our knowledge, no prior work had been conducted where diamond shaped Fe_3O_4 nanoparticles were incorporated into δ-MnO_2 nanoflowers in a hierarchical fashion. In order to investigate the extent of Fe_3O_4 nano-diamonds in increasing the electrochemical performance of δ-MnO_2 nanoflowers, three nanocomposites, *i.e.*, δ-MnO_2/(1%) Fe_3O_4, δ-MnO_2/(3%)Fe_3O_4, and δ-MnO_2/(5%) Fe_3O_4 were synthesized using a facile hydrothermal method. After synthesizing Fe_3O_4 nano-diamonds, they were added to the precursor solution of δ-MnO_2 nanoparticles in different weight percentages (% w/w), to prepare nanostructured composite samples. Then, these nanocomposites and a sample of pure δ-MnO_2 nanoflowers were characterized by electrochemical measurements to evaluate the optimized level of Fe_3O_4 content in terms of the electrochemical performance of the material.

Materials and methods

Materials

For hydrothermal synthesis of δ-MnO_2 nanoflowers, potassium permanganate ($KMnO_4$) and manganese sulfate ($MnSO_4$) were used. And for Fe_3O_4 nanoparticles, iron(III) chloride hexahydrate ($FeCl_3{\cdot}6H_2O$), polyethylene glycol (PEG 8000), and hydrazine 64% (N_2H_4) were used. All reagents were 98% pure and obtained from Merck, India. The reagents were of analytical grade; therefore, no further purification was needed. Throughout the synthesis processes, deionized (DI) water was employed as solvent.

Synthesis of diamond shaped Fe_3O_4 nanoparticles

A solution of 80 mL DI-water, 0.028 mol $FeCl_3{\cdot}6H_2O$ and 0.0003 mol PEG was prepared by magnetic stirring for around 30 minutes. During the continuous stirring process, 9 mL of N_2H_4 was added dropwise, resulting in a dark brown solution. It was then immediately transferred to a Teflon-lined autoclave and heated at 160 °C in an oven for 4 hours. After natural cooling, the precipitate was centrifuged with DI-water and ethanol. After drying the precipitate at 60 °C for 24 hours, the final Fe_3O_4 nanoparticles were obtained.[48]

Synthesis of δ-MnO_2 nanoflowers

First of all, 0.00631 mol of $MnSO_4{\cdot}H_2O$ was dissolved in 80 mL of DI-water and stirred vigorously to obtain a clear solution. Then, 0.0169 mol $KMnO_4$ was added to the solution while it was continuously stirred for about 15 more minutes. As soon as the solution became homogeneous, it was transferred to a Teflon-lined autoclave and heated in the oven at 140 °C for 30 minutes. The resulting precipitate was collected by centrifuging the suspension and washed with DI-water and ethanol. The final material was obtained after drying the cleaned precipitates at 60 °C for 10 hours.

Synthesis of δ-MnO_2 nanoflower–Fe_3O_4 nano-diamond composites

To synthesize δ-MnO_2/(1 wt%) Fe_3O_4, a solution of 80 mL DI-water, 0.00631 mol of $MnSO_4{\cdot}H_2O$ and 0.0169 mol $KMnO_4$ was vigorously stirred for 30 minutes. Then, an appropriate amount of previously synthesized Fe_3O_4 nano-diamonds was added to the solution and sonicated for 30 minutes to make the suspension homogeneous. After that, the suspended solution was immediately transferred to a Teflon-lined autoclave which was then put into the oven at 140° for 30 minutes. The primarily obtained material was separated by centrifuging, washed with ethanol and DI-water several times and dried at 60° for 24 hours to obtain the δ-MnO_2/(1 wt%) Fe_3O_4 nanocomposite. In a similar process, different amounts of Fe_3O_4, *i.e.*, 3% and 5 wt% were used to obtain δ-MnO_2/(3 wt%) Fe_3O_4 and δ-MnO_2/(5 wt%) Fe_3O_4 nanocomposites, respectively. The synthesis procedure is schematically illustrated in Fig. 1.

Fig. 2 illustrates the nanoflowers of pure δ-MnO_2 and δ-MnO_2/Fe_3O_4 nanocomposites. MnO_2 nanoflowers are formed by numerous nano-petals. In nanocomposites, the MnO_2 nanoflowers contain diamond-shaped Fe_3O_4 nanoparticles possibly buried in them. When the Fe_3O_4 content is increased to 5%, its nanoparticles protrude from the surface of δ-MnO_2 nanoflowers and hamper the growth of δ-MnO_2 nano-petals in those regions.

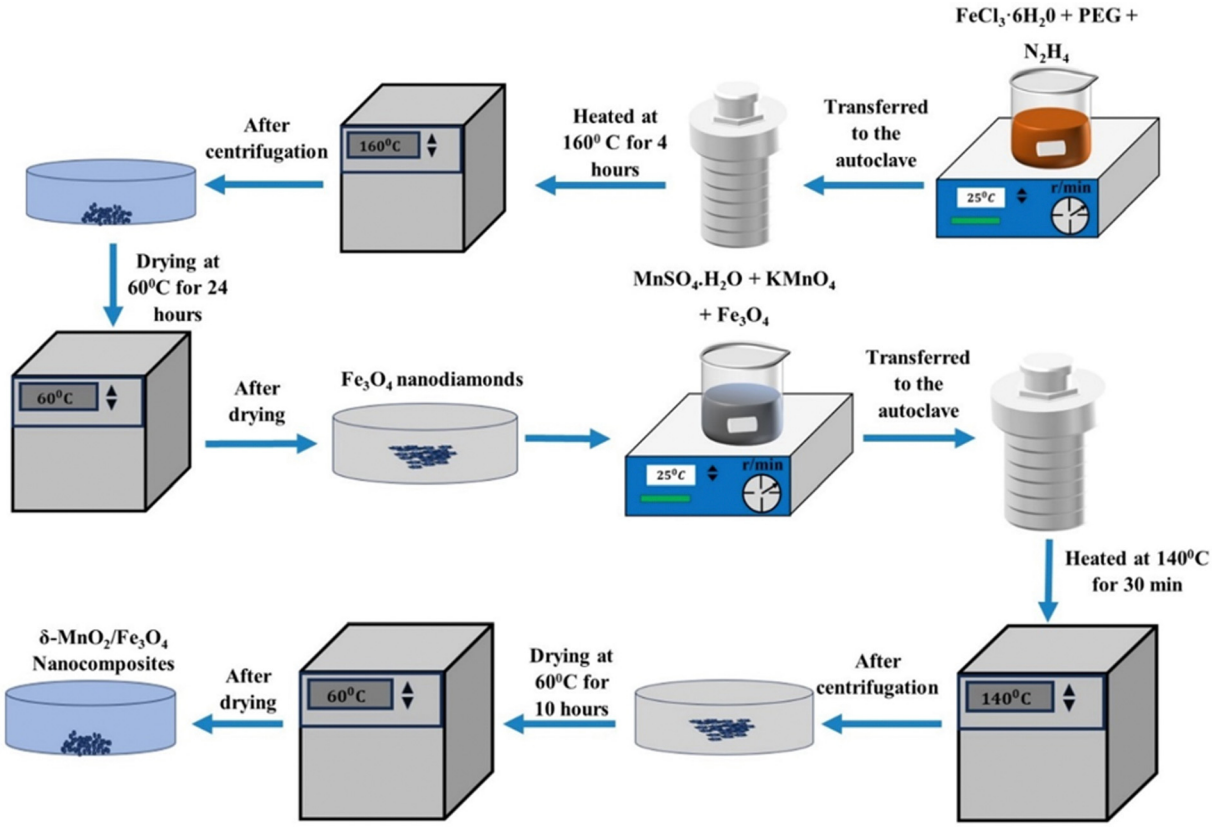

Fig. 1 Flowchart showing δ-MnO_2/Fe_3O_4 nanocomposite synthesis process. After synthesizing Fe_3O_4 nanodiamonds, it is mixed into the precursor solution of δ-MnO_2 nanoflowers at 1, 3 and 5 wt% producing δ-MnO_2/(1%) Fe_3O_4, δ-MnO_2/(3%) Fe_3O_4 and δ-MnO_2/(5%) Fe_3O_4 nanocomposites, respectively.

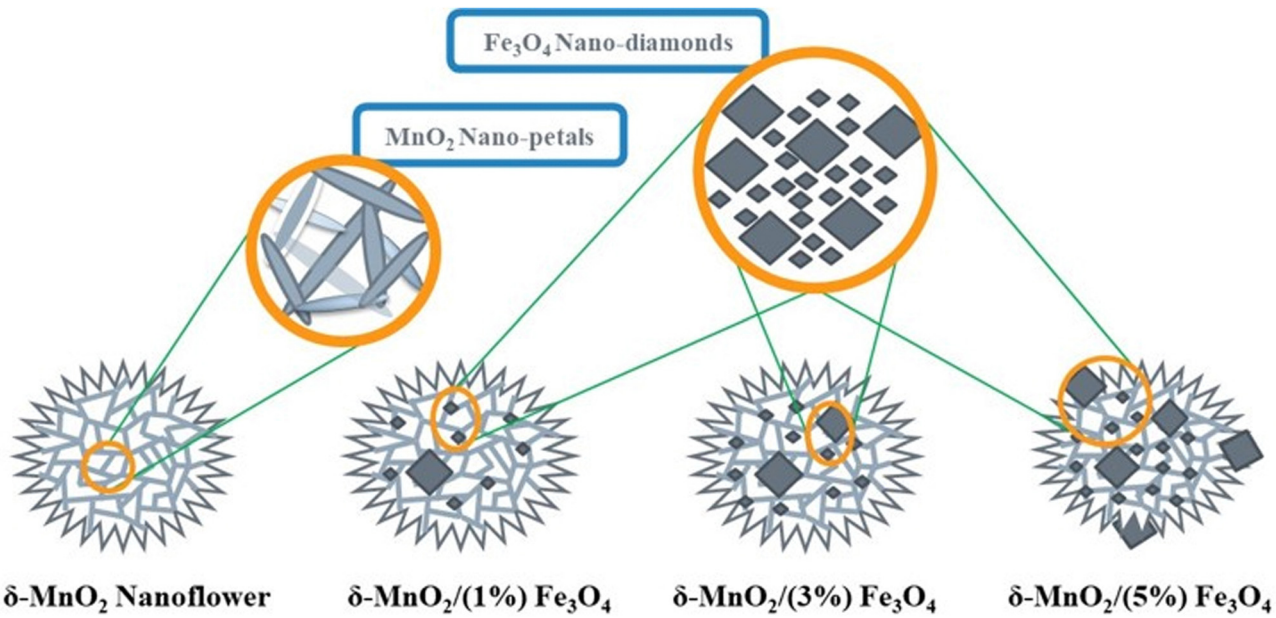

Fig. 2 A schematic Illustration of the morphologies of the synthesized pure δ-MnO_2 and δ-MnO_2/Fe_3O_4 nanocomposites. δ-MnO_2 nanoflowers are organized alignment of numerous nano-petals. Fe_3O_4 nanoparticles grew in large and small diamond shapes. At higher wt% (~5%), Fe_3O_4 nano-diamonds protrude the surface of δ-MnO_2 nanoflowers, hampering the nano-petal formations.

Electrode preparation

To create working electrodes, a slurry of active material was deposited onto a defined area (0.3 cm^2) of a glassy carbon electrode. This slurry was prepared by blending the active material (96%) with poly vinyl alcohol (PVA, 4%) and dimethyl sulfoxide, followed by sonication for an hour. After deposition, the working electrodes were dried at 65 °C for several hours. In this process, PVA serves as a binder, as its hydroxyl groups help to form hydrogen bonds between the glassy carbon electrode and the active materials.[49,50] Meanwhile, dimethyl sulfoxide is a polar aprotic solvent and capable of dissolving both polar and non-polar compounds.

Characterization

For the purpose of crystallographic analysis, the X-ray diffraction (XRD) patterns of the nanoparticles (NPs) were obtained over a 2θ range of 10°–70° using an X-ray diffractometer (PANalytical Empyrean) equipped with a Cu-Kα X-ray source ($\lambda_{CuK\alpha}$ = 1.54278 Å). A silicon zero background holder was used to place the powder samples. The sample surface was accurately aligned with the diffraction plane and the sample was rotated at 60 rpm during diffraction pattern acquisition adopting a reflection-transmission spinner module as the sample stage to maintain a uniform irradiation area both at low and high X-ray incident-angles. The adopted scan speed was 0.041683° per second in continuous scanning mode of operation. Surface morphologies were investigated using a field emission scanning electron microscope (JEOL JSM 7600F). High resolution transmission electron microscopy (HR-TEM) was carried out by using a JEOL JEM 2100 F transmission electron microscope to study the micromorphology of δ-MnO_2/Fe_3O_4 nanocomposites. The material was dispersed into a small amount of ethanol and sonicated for 20 minutes. The sonicated sample was then placed on a carbon-coated 3 mm Cu grid and inserted into the microscope after drying for microstructural analysis. The electrochemical performance of electrodes comprising pure MnO_2 nanoflowers and MnO_2 nanoflowers with varying proportions of Fe_3O_4 was examined using a CS310 electrochemical workstation (Corrtest) in a 0.5 M Na_2SO_4 electrolyte with a three-electrode configuration. The working electrode was a glassy carbon electrode, the reference electrode was Ag/AgCl, and the counter electrode was a platinum plate measuring 1 cm × 1 cm area. The electrochemical measurements were conducted by cyclic voltammetry (CV), galvanostatic charge–discharge (GCD), and electrochemical impedance spectroscopy (EIS) in a 0.5 M Na_2SO_4 aqueous solution. The potential window for CV and GCD analysis was from −0.2 V to 0.7 V with scan rates of 20, 40, 60, 80 and 100 mV s^{-1}. The EIS measurements were conducted using a sinusoidal bias voltage over a frequency range from 0.1 to 10^5 Hz.

Results and discussion

X-ray diffraction (XRD)

The crystallographic structures of both δ-MnO_2 and δ-MnO_2/Fe_3O_4 composites were examined using the X-ray diffraction (XRD) technique. Fig. 3 displays the XRD patterns obtained for δ-MnO_2 nanoflower and δ-MnO_2/Fe_3O_4 nanocomposites. The observed XRD peaks for pristine δ-MnO_2 nanoflowers correspond to the JCPDS card number 80–1098, with diffraction peaks indexed as (001), (002), ($\bar{1}$11), and (020) reflections.[51] The peak marked with asterisks (*) in the nanocomposites corresponds to the (311) plane of diamond Fe_3O_4 nanoparticles.[48] The diffractograms exhibit a notably high noise-to-signal ratio. The weak and diffuse XRD peaks indicate the inferior crystallinity of the synthesized δ-MnO_2 nanostructure. However, the most intense peak, denoted as (001), signifies a well-stacked interlayer distance along the c axis, which is a feature that has been documented for other birnessites.[52] An additional peak observed in the diffractograms of δ-MnO_2/Fe_3O_4 nanocomposites at a 2θ value of 37° corresponds to Fe_3O_4 nanodiamonds which is regarded as the reflection with the highest relative intensity in polycrystalline Fe_3O_4. However, no other peaks of Fe_3O_4 are evident in the diffraction patterns of the δ-MnO_2/Fe_3O_4 nanocomposites, which can be attributed to a relatively minute amount of Fe_3O_4 nanodiamonds in the composites. The peak position shifted to lower angles when Fe_3O_4 nanodiamonds were added to δ-MnO_2, as indicated by the dotted line in Fig. 3.[53–55] This peak shift may be attributed to uniform strain caused by defects like interstitial incorporation of Fe^{2+}/Fe^{3+} into the MnO_2 lattice possibly leading to a reduction in the average crystallite size, which decreases with the addition of Fe_3O_4 nanodiamonds, as shown in Fig. 3.[56] The possible migration of Fe ions across the δ-MnO_2/Fe_3O_4 interface due to incorporation of Fe_3O_4 nanodiamonds into δ-MnO_2 nanoflowers could cause the following reactions to occur, leading to crystal defect formation:

Vacancies:

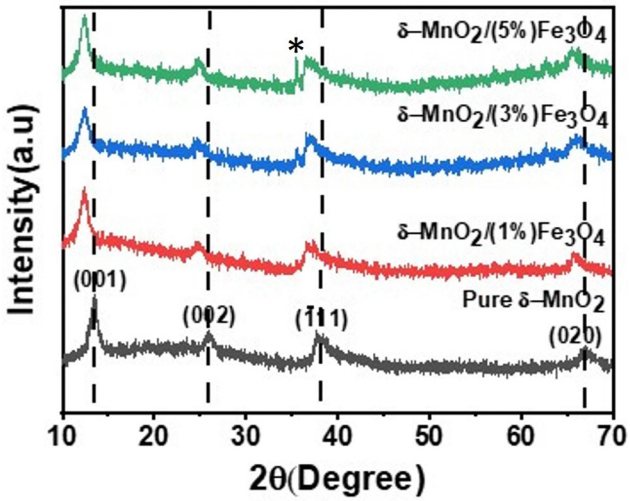

Fig. 3 XRD patterns of pure δ-MnO_2 nanoflower and δ-MnO_2/Fe_3O_4 nanocomposites. The asterisk corresponds to (311) peak from Fe_3O_4 nanodiamond and its intensity increases with increase in Fe_3O_4 content.

$$\frac{1}{2}Fe_2O_3 \underset{MnO_2}{\longrightarrow} Fe'_{Mn} + V_O^{\bullet\bullet} \quad (1)$$

$$\mathrm{FeO} \underset{\mathrm{MnO_2}}{\longrightarrow} \mathrm{Fe''_{Mn}} + \mathrm{V_O^{\bullet\bullet}} \quad (2)$$

Interstitials:

$$\mathrm{Fe_3O_4} \underset{\mathrm{MnO_2}}{\longrightarrow} \mathrm{Fe_i^{3+}/Fe_i^{2+}} + \mathrm{e'} \quad (3)$$

The formation of oxygen vacancies due to the incorporation of Fe_3o_4 nanodiamonds in δ-MnO_2 nanoflowers as indicated by the above reactions (1) and (2) can be confirmed by the EDX spectra as shown in Fig. SF1 (ESI†). Here the rise in the Mn/O atom % ratio of all nanocomposites above the ratio of 0.5 for pristine MnO_2 as shown in Fig. SF2 (ESI†) (obtained from EDX spectral analyses) suggests the presence of lattice oxygen vacancies. The highest Mn/O ratio of MnO_2/(3%) Fe_3O_4 indicates the highest concentration of oxygen vacancy present within the matrix lattice of the composite among all samples. These vacancies alter the local electronic environment around the manganese atoms. Moreover, a possible change in the oxidation state of manganese (Mn) in MnO_2 due to the formation of oxygen vacancies can be represented by the following reaction:

$$\mathrm{MnO_2} \rightarrow \mathrm{MnO_{2-x}} + x\mathrm{Mn^{3+}} + \frac{x}{2}\mathrm{O_2} \uparrow \quad (4)$$

In stoichiometric MnO_2, manganese is typically in the +4 oxidation state. When oxygen vacancies are introduced, some of the Mn^{4+} ions may reduce to Mn^{3+} to maintain charge neutrality in the crystal structure, leading to a mixed-valence state of Mn, typically observed as a combination of Mn^{4+} and Mn^{3+} states. Such a change in the oxidation state could contribute to enhance electronic conductivity and redox reaction culminating in an increment in the specific capacitance.[57] However, it is to be noted that the formation of the reduced state of Mn ions following reaction (4) requires oxygen expulsion from the lattice through evaporation, which is indeed a relatively high temperature process. Here, neither the synthesis process nor the electrochemical measurement involves temperature greater than 200 °C. Therefore, it can reasonably be presumed that the reduction of Mn ions through formation of anionic vacancies is negligible and the oxygen vacancies are primarily expected to form by the substitution reactions (1) and (2). Moreover, a slight decrease in the intensity of the diffraction peaks is noted upon the inclusion of Fe_3O_4 nanodiamonds. Such modification, in general, suggests a decline in the crystallinity of δ-MnO_2 as shown in Fig. 4, a phenomenon that can possibly be linked to the size effect, lattice distortion due to the presence of defects, and distinct pressure stress exerted by the Fe_3O_4 nanoparticles. Now such diminution in % crystallinity (ψ) of δ-MnO_2/Fe_3O_4 nanocomposites compared to the pristine δ-MnO_2 nanoparticles can be obtained from the following equation:

$$\psi = \frac{\sum_{i=1}^{n} \int_{\Theta_i} I(\Theta)\mathrm{d}\Theta}{\int_{\Theta_{\mathrm{full}}} I(\Theta)\mathrm{d}\Theta} \quad (5)$$

where $\Theta \equiv 2\theta$, n is the total number of (hkl) reflection, Θ_i is the angular dispersion of ith (hkl) reflection in the 2θ scale, Θ_{full} is the full angular range of the diffraction pattern and $I(\Theta)$ is the X-ray intensity at an angle Θ. The average crystallite size (L) of the sample was determined from the (001) peak by using the Scherrer formula,[58]

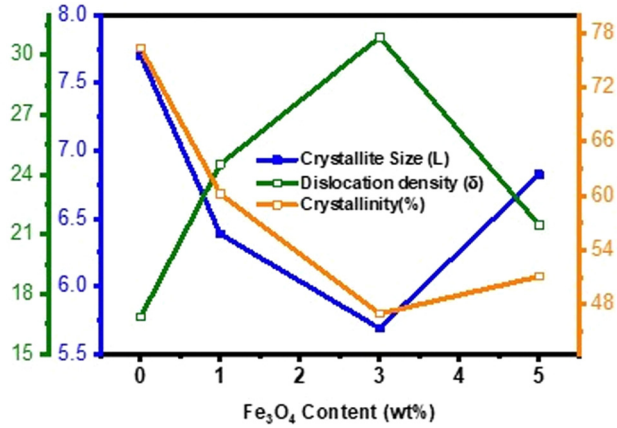

Fig. 4 Variation of crystallite size (L), dislocation density (δ) and % crystallinity (ψ) of pure δ-MnO_2 nanoflower and δ-MnO_2/Fe_3O_4 nanocomposites obtained from XRD line profile analysis as function of Fe_3O_4 content. The 3% incorporation of Fe_3O_4 nanodiamonds results in the highest dislocation density, smallest crystallite size and lowest % of crystallinity.

$$L = \frac{0.94\lambda}{\beta\cos\theta} \quad (6)$$

where λ is the wavelength of the X-ray used, θ is the incident angle for an (hkl) reflection and β is the instrument corrected full width at half-maximum of the diffraction peak. The dislocation density (δ) of the δ-MnO_2/Fe_3O_4 composites was calculated using the following equation,[59]

$$\delta = \frac{1}{L^2} \quad (7)$$

Fig. 4 illustrates the variation of structural parameters with the diamond shaped Fe_3O_4 nanoparticle content in δ-MnO_2 nanoflowers. The inclusion of the diamond shaped Fe_3O_4 nanoparticles initially leads to an ∼26% reduction in average crystallite size up to 3% Fe_3O_4 in the nanocomposite compared to pure δ-MnO_2. However, beyond 3% Fe_3O_4, there is an ∼20% increase in average crystallite size for 5% Fe_3O_4. Fig. 4 also shows the change in crystallinity due to the inclusion of diamond shaped Fe_3O_4 nanoparticles into δ-MnO_2 nanoflowers. The generation of disorderness is attributed to crystal imperfections, vacancies, and dislocations. It was observed that crystallinity decreased about ∼39% with the Fe_3O_4 content up to 3% compared to pristine δ-MnO_2; however, further increase of its content led to 9% rise of crystallinity from δ-MnO_2/(3%) Fe_3O_4, consequently resulting in an increase in the average crystallite size. The dislocation density and inverse of crystallinity serve as a measure of imperfections within the prepared samples. Fig. 4 shows that the dislocation density and crystallinity of the δ-MnO_2/Fe_3O_4 nanocomposites exhibit an opposite trend. The incorporation of diamond shaped Fe_3O_4 nanoparticles into the δ-MnO_2 nanoflowers induced lattice

distortion. This distortion led to the expansion of the interlayer distance, potentially facilitating rapid electron and ion transportation from the surface to the electrode.[60] Moreover, the presence of structural defects within the crystals could impede the stacking of the crystallographic layers of δ-MnO_2 nanopetals, leading to an increase in the inter-planar distance. This effect, combined with the modification in crystallite size, lattice distortion, crystal defects, and dislocation density, results in an alteration of the *d*-spacing.

Collectively, these factors favor the enhancement of the surface area of the nanocomposites, introduction of new active sites, and improvement of the intercalation/deintercalation kinetics of the charge carriers during the charging/discharging process.[61–64] Nonetheless, among all the samples, δ-MnO_2/(3%) Fe_3O_4 exhibits the lowest crystallite size, poorest crystallinity, highest dislocation density and crystal defects, and the widest interplanar spacing. These are the potential facilitators for enhanced charge transportation and improved electrochemical performance of this nanocomposite.[60,65]

Scanning electron microscopy (SEM)

In Fig. 5(a), the FE-SEM micrograph of Fe_3O_4 nanoparticles is displayed. Due to the resemblance with the diamond shape, these particles of Fe_3O_4 were addressed as nano-diamonds. The Fe_3O_4 particles exhibit two distinct size distributions: the small particles (>80% in terms of the particle number) were ∼40–50 nm, whereas the large ones (<20% in terms of the particle number) were ∼300–350 nm. Fig. 5(b) and (c) show the micrographs of pristine δ-MnO_2 nanostructured particles at different magnifications. δ-MnO_2 particles exhibited a flower-like structure, made of numerous nano-petals. The nano-petals were attached with one another in a hierarchical manner, giving rise to flower-like structures. The hierarchical nanostructure is something where the nanoscale sub-units are aligned in a well-organized manner. Here, the 2D nano-petals aligned with one another to form 3D flower like patterns.[66] Nonetheless, in the micrograph in Fig. 5(b), the nanoflowers can be seen to have formed clusters. The average diameter of the nanoflowers is ∼680 nm and the average thickness of the nano-petals is ∼17 nm. In Fig. 5(d), the micrograph of the δ-MnO_2/(1%) Fe_3O_4 nanocomposite is shown. Since the % (w/w) of Fe_3O_4 is very little, it appears that this micrograph is quite similar to that of the pristine δ-MnO_2 nanoflowers. However, the average thickness of the nano-petals slightly increased to ∼18 nm. The micrograph of δ-MnO_2/(3%) Fe_3O_4 is shown in Fig. 5(e), where δ-MnO_2 nanoflowers are retained without any visible distortion despite the increase in the amount of Fe_3O_4 nano-diamonds. It appears that the Fe_3O_4 nano-diamonds took positions in between the nano-petals of δ-MnO_2 nanoflowers. However, the average thickness of nano-petals decreased by ∼3 nm up to 3% Fe_3O_4. Upon further increase in the wt% of the Fe_3O_4 nano-diamonds, some of their larger particles protrude from the surface of the δ-MnO_2 nanoflowers, as evident in Fig. 5(f). This bulging out of the Fe_3O_4 nano-diamonds from the interior of the δ-MnO_2 nanoflowers hampers the growth of nano-petals, causing some visible distortions in the surface regions. Furthermore, their average thickness reduces to ∼13 nm.

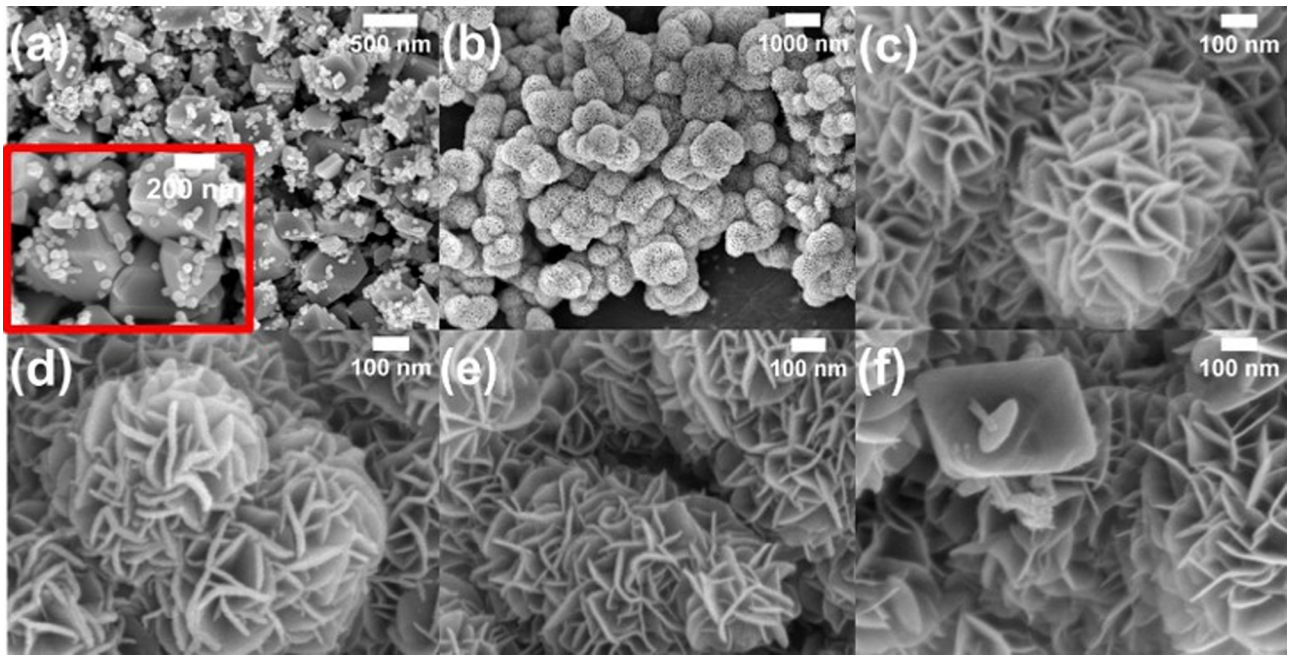

Fig. 5 FE-SEM Micrographs of (a) Fe_3O_4 nano-diamonds (inset shows the magnified image of (a)), (b) and (c) pristine δ-MnO_2 nanoflowers at different magnifications, where the nano-petals were attached with one another in a hierarchical manner, (d) δ-MnO_2/(1%) Fe_3O_4 nanocomposite (e) δ-MnO_2/(3%) Fe_3O_4 nanocomposite, (f) δ-MnO_2/(5%) Fe_3O_4 nanocomposite. The micrographs of 1% and 3% Fe_3O_4 incorporated δ-MnO_2 nanocomposites look similar to pristine δ-MnO_2 nanoflowers due to the small amount of Fe_3O_4 addition. The nanodiamonds protrude from the surface of the δ-MnO_2 nanoflowers when Fe_3O_4 is added beyond 3%.

Besides, the Mn/O atom % ratio obtained from the semi-quantitative EDX spectra in Fig. SF1 (ESI†) clearly exhibits a variation with the addition of diamond shaped Fe_3O_4 as shown in Fig. SF2 (ESI†). The ratio is ~0.5 in MnO_2 as shown in Fig. SF2 (ESI†), indicating the stoichiometric proportion of Mn and O in this compound. However, the MnO_2/(3%) Fe_3O_4 nanocomposite shows the highest ratio of ~1.04 among all nanocomposites. The value of the ratio above 0.5 suggests a deviation from the typical oxygen stoichiometric composition of MnO_2, indicating a relative oxygen deficiency. This deficiency is accommodated by the formation of oxygen vacancies within the matrix lattice, which indicates the dominance of anionic defects in the crystal structure.[67]

Transmission electron microscopy (TEM)

Fig. 6(a) shows the TEM image of pure δ-MnO_2 nanoflowers. These nanoflowers are made up of an assembly of numerous nano-petals, which stack with one another, growing from a central region to radially outward direction in a hierarchical manner. As in the inset of Fig. 6(a), petal like nanostructures seem to originate from a nanoflower core.[68] Besides, the nanopetals were observed to overlap each other due to their nanosized thickness.[69,70] Fig. 6(b) shows the lattice fringes of δ-MnO_2 nanopetals having a lattice spacing of 0.72 nm which corresponds to the (001) plane of the monoclinic phase, in accordance with JCPDS card: 80–1098.[51] Fig. 6(c)–(e) shows the HRTEM images of δ-MnO_2/Fe_3O_4 nanocomposites and from the HRTEM image the lattice spacing corresponding to the (001) planes of δ-MnO_2 are found to be 0.75 nm, 0.76 nm, and 0.75 nm for 1%, 3%, and 5% of Fe_3O_4, respectively indicating that incorporation of Fe_3O_4 nanoparticles suddenly increases the lattice spacing of the composite as shown in Fig. 6(f). This widening of the lattice spacing can be attributed to the generation of defects in the δ-MnO_2 crystal structure due to the incorporation of Fe_3O_4 as mentioned before. These defects shorten the path of electrolyte ions by providing accessible storage sites. Additionally, the increased interlayer spacing may prevent the collapse of the crystallographic layers during rapid charge–discharge operations.[71] The porous surface of the hydrothermally produced δ-MnO_2/Fe_3O_4 nanocomposite, along with its broad interlayer spacing and increased specific surface area, may contribute to enhanced capacitance.[72]

Electrochemical performance analysis

Cyclic voltammetry (CV)

To investigate the charge storage mechanism of pure δ-MnO_2 and Fe_3O_4 nanodiamond incorporated δ-MnO_2, cyclic voltammetry (CV) was conducted. Fig. 7(a) displays the CV curves of all the nanocomposites at a specific scan rate of 60 mV s^{-1}. Fig. 7(b) shows the graphical trend of the area calculated from the CV loops of Fig. 7(a). It is observed that the inclusion of Fe_3O_4 nano-diamonds increased the area of CV curves, with δ-MnO_2/(3%) Fe_3O_4 nanocomposite exhibiting the largest area.

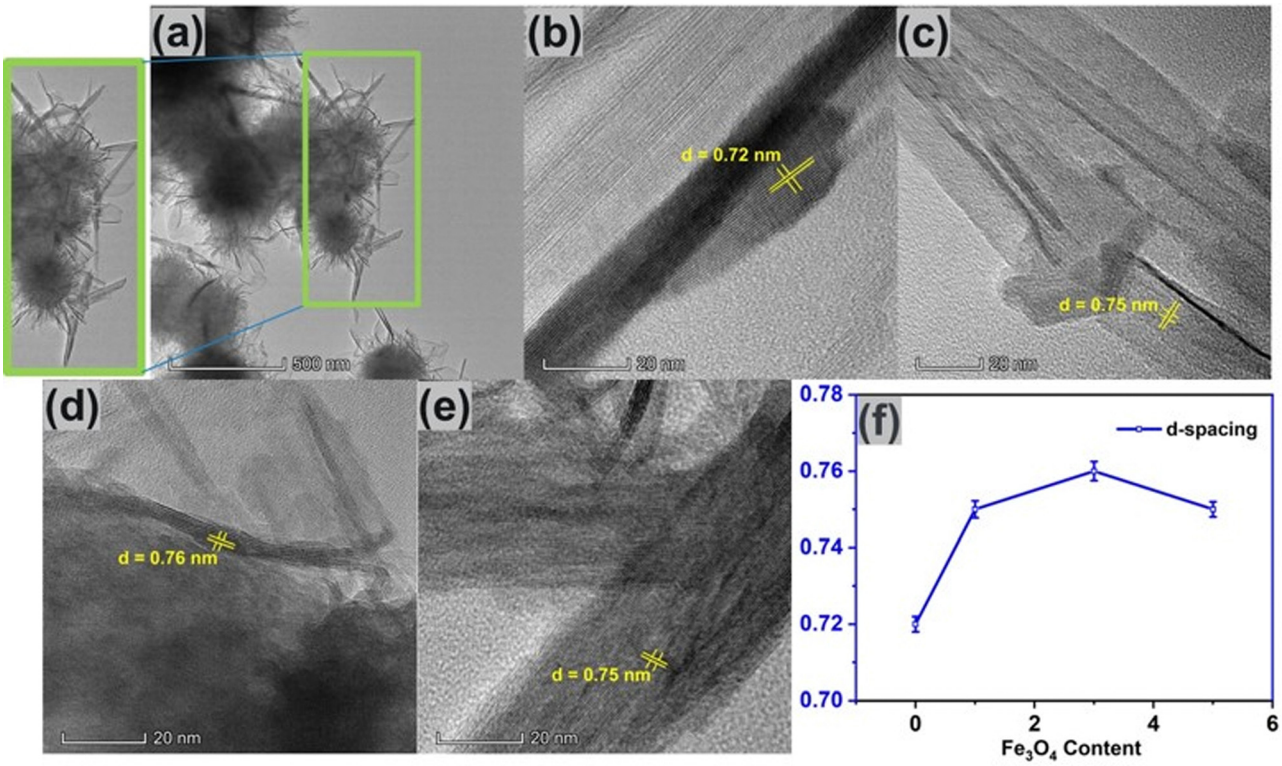

Fig. 6 (a) TEM image of δ-MnO_2 nanoflower. HR-TEM images of (b) pure δ-MnO_2, (c) δ-MnO_2/(1%) Fe_3O_4, (d) δ-MnO_2/(3%) Fe_3O_4, (e) δ-MnO_2/(5%) Fe_3O_4, (f) variation of *d*-spacing with respect to Fe_3O_4 content. Here, the observed increase in lattice spacing with Fe_3O_4 content can be attributed to the generation of defects possibly due to the incorporation of Fe ion into the δ-MnO_2 lattice.

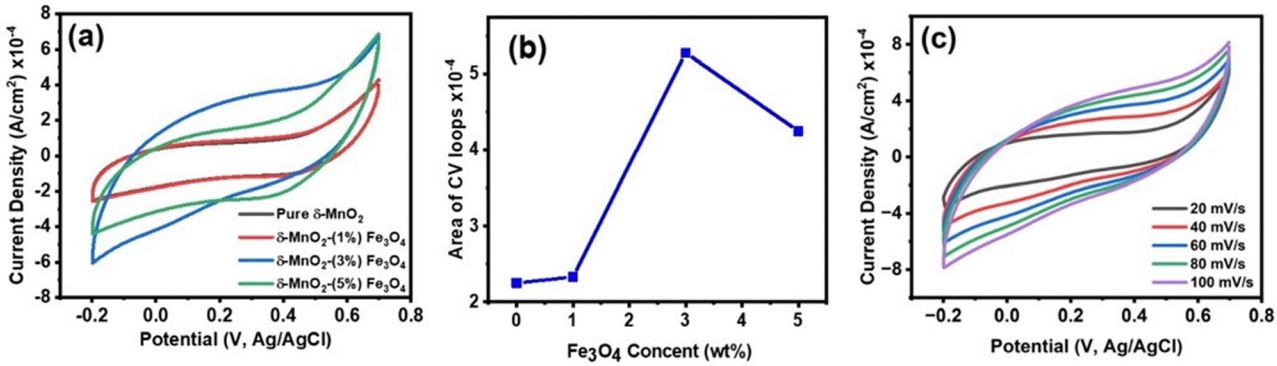

Fig. 7 (a) Cyclic voltammetry (CV) loops of δ-MnO_2 nanoflower and δ-MnO_2/Fe_3O_4 nanocomposites at 60 mV s^{-1} scan rate; (b) area of the CV loops as the function of Fe_3O_4 content, calculated from 7 (a); (c)CV loops δ-MnO_2/(3%) Fe_3O_4 nanocomposite at scan rates of 20 to 100 mV s^{-1}; the shape of the CV curves indicates the presence of electric double layer capacitance (EDLC) and pseudocapacitance. The incorporation of Fe_3O_4 nano-diamonds improved the specific capacitance of δ-MnO_2 nanoflowers, with the δ-MnO_2/(3%) Fe_3O_4 nanocomposite exhibiting the widest CV curve and hence, the best performance.

Therefore, the incorporation of Fe_3O_4 nano-diamonds can be attributed for the improvement of specific capacitance of δ-MnO_2 nanoflowers.[73] However, when the Fe_3O_4 nano-diamond content is increased to 5%, the area of the cyclic voltammetry (CV) curve decreases, causing a possible reduction in specific capacitance of δ-MnO_2. As it has been shown that at high Fe_3O_4 content (~5%), some of the Fe_3O_4 nano-diamonds protrude the surface of δ-MnO_2 nanoflowers (Fig. 5(f)), hampering nanopetal formations in those regions. This could adversely affect the surface area of δ-MnO_2 nanoflowers and in turn, its specific capacitance.

Since the δ-MnO_2/(3%) Fe_3O_4 nanocomposite exhibited the best performance, further CV measurement was conducted on this sample at different scan rates as depicted in Fig. 7(c). The quasi-rectangular shape of the CV curves, irrespective of scan rate suggests that both of electric double-layer capacitance (EDLC) effect and pseudocapacitance mechanism are possibly active for charge storage process.[74] Pseudocapacitance could arise through processes including underpotential deposition, intercalation and surface redox reactions. In the underpotential deposition mechanism, alkali cations are adsorbed onto or desorbed from the electrode/electrolyte interface, *via* a surface process, such as:

$$(\delta\text{-MnO}_2)_{\text{surface}} + \text{Na}^+ + \text{e}^- \leftrightarrow (\delta\text{-MnO}_2 \cdot \text{Na})_{\text{surface}} \quad (8)$$

For highly disordered materials, this process predominates, as evidenced by the CV curve in Fig. 7(c), where the underpotential deposition involves the adsorption/desorption of Na^+ ions across the interface between the electrolyte and the surface of the nanostructured δ-MnO_2.[75]

The second mechanism involves the intercalation or extraction of alkali cations (Na^+) from the electrolyte into the bulk of the δ-MnO_2 nanostructure. SEM images in Fig. 5 exhibit that the surfaces of pure δ-MnO_2 nanoflowers and δ-MnO_2/Fe_3O_4 nanocomposites possess a nanoporous structure which is suitable to facilitate the intercalation process of Na^+ ions by increasing specific surface area for intercalation to take place.[76–79] The intercalation process can be shown by following equation:

$$(\delta\text{-MnO}_2)_{\text{surface}} + \text{Na}^+ + \text{e}^- \leftrightarrow (\delta\text{-MnOONa})_{\text{intercalation}} \quad (9)$$

The fast and reversible successive surface redox reactions of pristine δ-MnO_2 and δ-MnO_2/Fe_3O_4 nanocomposites are facilitated by the intercalation/de-intercalation process. Here, Fe^{2+} ions can donate electrons to become Fe^{3+} and the sulphate anions from the electrolyte solution intercalate into the crystallographic layers of δ-MnO_2 nanopetals to balance the charge of the cations. Meanwhile, Na^+ and H^+ ions from the solution also intercalate into the crystallographic layers to receive the donated electrons.[45] Both processes produce conjugates, as represented by the following equations:

$$\delta\text{-MnO}_2 + \text{H}^+ + \text{Na}^+ + 2\text{e}^- = \text{MnOOHNa} \quad (10)$$

$$2\text{Fe}^{\text{II}}\text{O} + \text{SO}_4^{2-} \leftrightarrow (\text{Fe}^{\text{III}}\text{O})^+\text{SO}_4^{2-}(\text{Fe}^{\text{III}}\text{O})^+ + 2\text{e}^- \quad (11)$$

In Fig. 7(c), as the scan rates increased from 20 to 100 mV s^{-1}, the response curves of the δ-MnO_2/(3%) Fe_3O_4 nanocomposite electrode gradually get distorted to a spindle-like shape. At low scan rates, the electrolyte ions get ample of time to diffuse towards the electrode surface. Thereby, the ions can thoroughly penetrate the surface of δ-MnO_2 nanoflowers and utilize the active sites of the porous infrastructure of its nano-petal assembly. As a result, large amount of charge can be stored through this interaction, increasing the specific capacitance of the material. Conversely, at higher scan rates, the time available for electrolyte ions to reach the surface as well as the deeper pores of δ-MnO_2 nanoflowers is reduced. Thereby, the ions are deprived of the opportunity to penetrate the internal surface area. They only get to interact with the active sites of the outer, more accessible surface, leaving the inner structure of the nanoflower underutilized for charge storage. Thus, the overall capacitance is affected.[80] Besides, at higher scan rates, the electrode potential changes abruptly. When the potential switches drastically, the electrode lags behind in terms of reaching equilibrium, leading to polarization. It slows down

the charge transfer mechanism between the material surface and the electrolyte which adversely affects the capacitance.[81–83]

Galvanostatic charge–discharge (GCD)

The supercapacitive characteristics of the material can also be assessed from galvanostatic charging–discharging (GCD) profiles. GCD curves offer better quantitative insights compared to CV curves of the materials, as galvanic charging–discharging process closely resembles the real-world applications. Fig. 8(a) displays the GCD curve of all samples at a specific current density of 0.3 A g^{-1} within a potential window of −0.2 to 0.7 V. The deviation of the GCD curve from the typical symmetrical triangular shape indicates the presence of a pseudocapacitive charge storage mechanism.[84] The pseudocapacitive behavior arises from the intercalation of Na^+ ions from the electrolyte onto the nanopetals of the nanoporous structured δ-MnO_2 nanoflowers, as explained by eqn (10) and (11). As mentioned before, the SEM images in Fig. 5 indicate the presence of a nanoporous surface structure of δ-MnO_2 nanoflowers and the δ-MnO_2/Fe_3O_4 nanocomposites. Such morphology favors the intercalation of Na^+ ions deep into the electrode material by enhancing the specific area for intercalation process to inititate.[85]

Fig. 8(b) illustrates the GCD curve of the δ-MnO_2/3% Fe_3O_4 nanocomposite at various current densities. It can be observed that the specific capacitance obtained from the GCD curves of the nanocomposite decreased with increasing current density (inset of Fig. 8(b)). Such a trend in specific capacitance is a common phenomenon, where at low current densities, electrolyte ions diffuse efficiently to all active sites of the electrode, facilitating complete insertion/extraction process and resulting in superior capacitance.[85] On the other hand, at higher current densities, ionic diffusion is predominantly restricted to the near-surface regions of the electrode, leading to lower capacitance due to relatively reduced charge transportation time.[86]

Fig. 9 shows the variation in specific capacitance, and discharge time of δ-MnO_2 and δ-MnO_2/Fe_3O_4 composites at a current density of 0.30 A g^{-1}. The specific capacitance (C_{sp}) was estimated from the GCD curves using the formula:[87]

$$C_{sp} = \frac{I\Delta t}{m\Delta V} \tag{12}$$

where m = mass of active materials, Δt = discharge time, I = discharge current, and ΔV = potential window. Fig. 9(a) shows that the specific capacitance of the synthesized material increases with the incorporation of up to 3% Fe_3O_4 nanodiamonds in pure δ-MnO_2. The δ-MnO_2/(3%) Fe_3O_4 nanocomposite gives a specific capacitance (459 F g^{-1}), which is about six times higher than that of pure δ-MnO_2. However, beyond this weight percentage, the specific capacitance decreases by more than half of the maximum value. As shown in Fig. 9(b), the δ-MnO_2/(3%) Fe_3O_4 nanocomposite exhibited the longest discharge time (1377 seconds) compared to pure δ-MnO_2 (228 seconds), δ-MnO_2/(1%) Fe_3O_4 (651 seconds), and δ-MnO_2/(5%) Fe_3O_4 (645 seconds), possibly indicating the highest level of Na^+ ion insertion into the δ-MnO_2/(3%) Fe_3O_4 nanostructure. The highest specific capacitance of δ-MnO_2/(3%) Fe_3O_4 may be due to smaller crystallite size, increased dislocation density, and higher disorder indicated by a gradual reduction in % crystallinity of δ-MnO_2 with increasing Fe_3O_4 content up to 3% (Fig. 4). The inclusion of Fe_3O_4 into δ-MnO_2 caused higher structural distortion and generated numerous defects and disordered states, which subsequently amplified the effective surface area for EDLC. Additionally, the gradual augmentation of lattice interlayer spacing of δ-MnO_2/Fe_3O_4 nanocomposites for up to 3% Fe_3O_4 incorporation substantially contributed towards the pseudocapacitance.[88–90] This

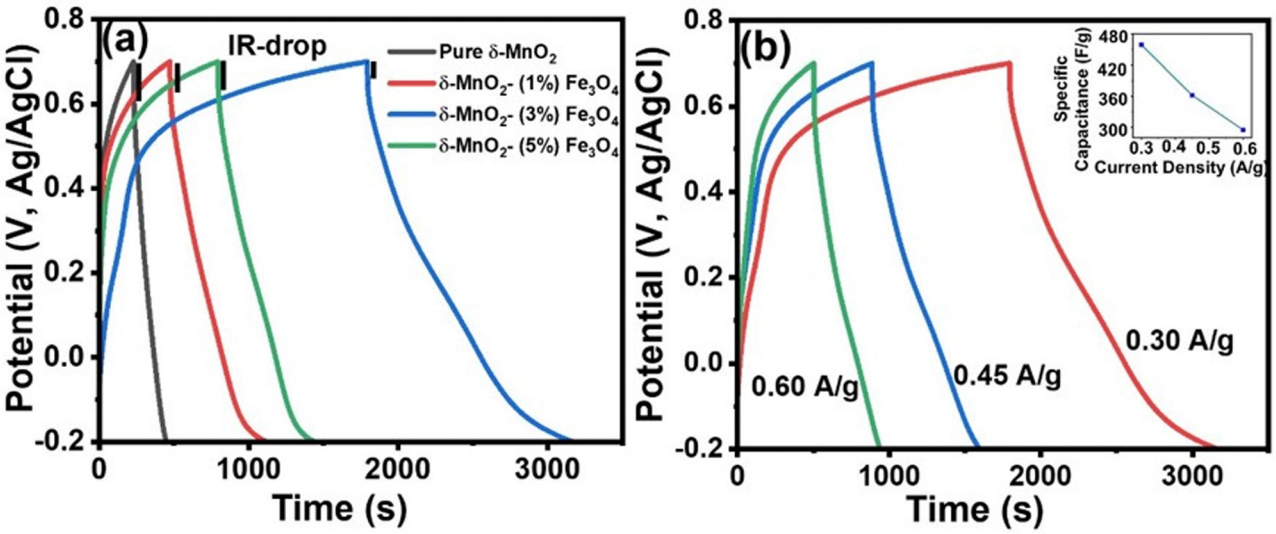

Fig. 8 (a) Galvanostatic charge–discharge (GCD) curves of δ-MnO_2 nanoflower and δ-MnO_2/Fe_3O_4 nanocomposites at current density of 0.30 A g^{-1}, (black vertical lines indicate the IR-drop of all electrode materials); (b) GCD curves of δ-MnO_2/(3%) Fe_3O_4 nanocomposite at different current densities. (The inset shows the variation of specific capacitance as a function of current density for the δ-MnO_2/(3%) Fe_3O_4 nanocomposite).

facilitated greater Na^+ ion insertion into the surface of the nanocomposites, enhancing their charge storage capability. However, both the crystallite size and crystallinity increased beyond 3% Fe_3O_4 content, thus reducing the overall capacitive performance in GCD measurements, as shown in Fig. 9(a), compared to the δ-MnO_2/(3%) Fe_3O_4 nanocomposite. In addition, in Fig. 8(a), at the onset of the discharge phase, a rapid drop in potential was observed, indicating energy losses due to internal resistance [4]. Notably, this abrupt potential drop (IR drop) is significantly smaller for the δ-MnO_2/Fe_3O_4 nanocomposite electrodes compared to the pure δ-MnO_2 electrode suggesting higher conductivity or reduced internal resistance due to the incorporation of Fe_3O_4 into δ-MnO_2 nanoflowers. Such reduction in internal resistance could be partly associated with the formation of structural defects like Fe-interstitials and oxygen vacancies possibly due to the incorporation of Fe-ions into the MnO_2 lattice as indicated in the XRD section. The enhancement in conductivity is advantageous for improving charge dynamics within the system. Compositing Fe_3O_4 nanodiamonds into pure δ-MnO_2 also reduced self-discharging phenomena, thereby leading to the minimal voltage drop and an increase in discharge time.[91]

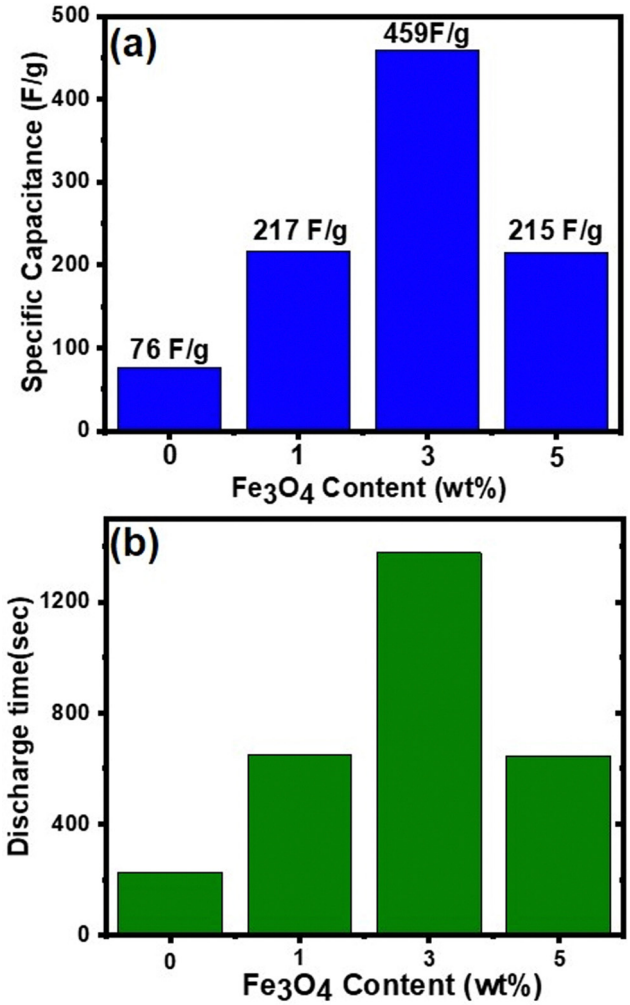

Fig. 9 (a) Specific capacitance of the samples as a function of Fe_3O_4 content, the δ-MnO_2/(3%) Fe_3O_4 nanocomposite shows the highest specific capacitance; (b) discharge time of the samples as a function of Fe_3O_4 content, obtained from the GCD curves in Fig. 8(a).

Electrochemical impedance spectroscopy (EIS)

The effect of conductivity and internal resistance on the trend of specific capacitance of the nanocomposites can be further supported by means of electrochemical impedance spectroscopic (EIS) analysis. The EIS measurement was performed to evaluate the resistive behavior and to understand the underlying mechanism of charge transfer of the pure δ-MnO_2 and the composite electrodes. Fig. 10 shows the fitted Nyquist plots of all prepared samples. The different regions provided by the Nyquist plot for the supercapacitor explain the charge-transfer-limited processes and the diffusion-limited processes. Conventionally, the so-called knee frequency can be used to separate the Nyquist plot into a high frequency semicircle and a low-frequency inclined line, as illustrated in Fig. 10. At the beginning of the half-circle, the non-zero intersection of the Nyquist plot with the real impedance axis gives the equivalent series resistance (R_s), which is a combination of interfacial resistance between the electrode and the current collector, the bulk resistance of the electrode, the internal resistance of the electroactive materials and the intrinsic ionic electrolyte resistance.[92] The double layer capacitance (C_{dl}) at the electrode/electrolyte interface and the charge transfer resistance (R_{ct}) are presented by the semicircle in the high-to-medium frequency range. And the inclined straight line (angled to the Z'-axis of the Nyquist plot) corresponds to the mass transfer resistance (Warburg impedance, Z_w). An equivalent impedance circuit (inset of Fig. 10) was formed to simulate the corresponding EIS spectra *via Z* View software to evaluate the different electrical components responsible for the observed electrochemical properties of the samples. Based on the

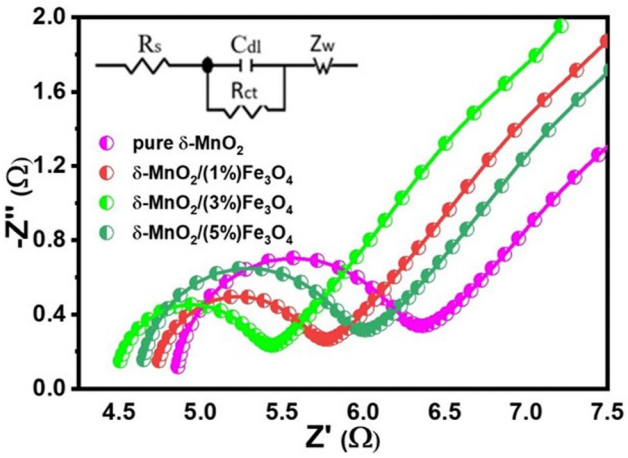

Fig. 10 EIS spectra of as-prepared pure δ-MnO_2 nanoflowers and δ-MnO_2/Fe_3O_4 nanocomposite electrodes. The inset shows equivalent Randle's circuit. Different electrical components of this circuit were obtained from fitting the experimental EIS spectra with Randle's circuit *via* Z View software.

proposed fitting circuit exhibited in inset of Fig. 10, the pure δ-MnO_2 electrode can be found to have the highest value of R_s (4.85 Ω) as shown in Table 1 and δ-MnO_2/(3%) Fe_3O_4 exhibits the lowest R_s value, possibly suggesting that the composite has a low contact resistance at the interface between the active material and the current collector and this contributes to rapid ion diffusion.[93] Additionally, the low R_s value also indicates a low internal resistance in δ-MnO_2/(3%)Fe_3O_4, which is supported by a relatively smaller IR drop observed in its GCD curve as shown in Fig. 8(a).[94] These EIS results also agree well with the CV results. The diameter of the semicircle is related to the charge transfer resistance, R_{ct} at the electrode–electrolyte interface. δ-MnO_2/(3%)Fe_3O_4 nanocomposite possesses the smallest diameter of the semicircle, indicating that δ-MnO_2/(3%)Fe_3O_4 has the lowest R_{ct} (0.87 Ω), as compared to δ-MnO_2, δ-MnO_2/(1%)Fe_3O_4 and δ-MnO_2/(5%)Fe_3O_4 as shown in Table 1. The insertion of Fe_3O_4 nanodiamonds into δ-MnO_2 nanoflowers could have a synergistic effect, increasing the effective surface area and defect states of the nanocomposites, facilitating a greater charge transfer rate at the electrode–electrolyte interface compared to pure δ-MnO_2.[95] The lowest R_{ct}, δ-MnO_2/(3%) Fe_3O_4 indicates that 3% Fe_3O_4 nanodiamond content optimizes the interface charge (electronic/ionic) transportation process. Nonetheless, further increase in the Fe_3O_4 content could essentially impedes the growth of nanopetals in those areas where Fe_3O_4 nanodiamonds protrude from the surface of δ-MnO_2 nano flowers. This reduces the effective surface area and hence, the surface redox reaction sites hampering the Na^+ intercalation process, partly overshadowing the benefits gained from the reduced charge transfer resistance.

All electrodes in the Nyquist plot exhibit a slope between 45° and 90° in the low-frequency range, indicating that the electrodes were operating with both capacitive and diffusion-controlled characteristics.[45] As the δ-MnO_2/(3%)Fe_3O_4 nanocomposite electrode exhibits a smaller slope and a lower Z_w value (6.9 Ω) than the remaining electrodes, as evident from the Warburg impedance values in Table 1, it could be a deemed to have superior ion diffusion rate capability than the other samples. Therefore, all of these results point towards the δ-MnO_2/(3%)Fe_3O_4 nanocomposite electrode having a faster charge transportation capability than others. Thus, the δ-MnO_2/(3%)Fe_3O_4 nanocomposite electrode exhibited the highest specific capacitance. The results from EIS agree well with those from CV and GCD analysis, clearly suggesting that the electrodes of the nanostructured composite materials have lower resistance compared to pure δ-MnO_2 nanoflower for charges to move between the electrolyte and electrode.

Table 1 Values of the fitted electrical parameters from the experimental EIS spectra of pure δ-MnO_2 and δ-MnO_2/Fe_3O_4 nanocomposites

Electrode	R_s (Ω)	R_{ct} (Ω)	Z_w (Ω)
Pure δ-MnO_2	4.85	1.35	12.3
δ-MnO_2/(1%) Fe_3O_4	4.72	0.95	9.7
δ-MnO_2/(3%) Fe_3O_4	4.48	0.87	6.9
δ-MnO_2/(5%) Fe_3O_4	4.63	1.25	8.4

Cyclic stability

Long-term cyclic stability is as important as specific capacitance for any supercapacitor-based device. In this study, the δ-MnO_2/(3%) Fe_3O_4 nanocomposite exhibited the highest specific capacitance among all samples. Therefore, it was subjected to repetitive GCD measurements to evaluate capacitance retention and coulombic efficiency over 4000 cycles, as shown in Fig. 11. The capacitance retention and coulombic efficiency were calculated by using the following equations:[96,97]

$$\text{Capacitance retention (\%)} = \frac{n\text{th cycle capacitance}}{\text{1st cycle capacitance}} \times 100 \quad (13)$$

$$\text{Coulombic efficiency, } \eta = \frac{t_{\text{discharge}}}{t_{\text{charge}}} \times 100 \quad (14)$$

The results in Fig. 11 indicate a 75% retention of the initial capacitance after 4000 charge/discharge cycles. Initially, cyclic retention decreased to around 63% within the first few hundred cycles but began to increase after 750 cycles, eventually stabilizing at 75% retention after 4000 cycles. Generally, a rise in capacitance in the composite could stem from the activation of active sites within the material after certain number of cycles.[98,99] Once activated, the electrochemically active materials become fully exposed to the electrolyte,[100] facilitated by improved wettability of the electrode surface over time, which is expected to enhance electrolyte diffusion.[101,102] These improvements are likely to contribute to the observed increase in capacitance throughout cycling. Additionally, the interaction with Na^+ ions may generate numerous defective or disordered sites, increasing the electrode's charge storage capacity over time by enhancing the effective interaction surface area.[103] Moreover, as seen in the SEM micrographs in Fig. 5, the flower-like morphology of δ-MnO_2 and its mesoporous features are proposed to contribute to the electro-activation process.[104]

Besides, the introduction of oxygen vacancies confirmed by EDX analysis as shown in Fig. SF2 (ESI†) can lead to the

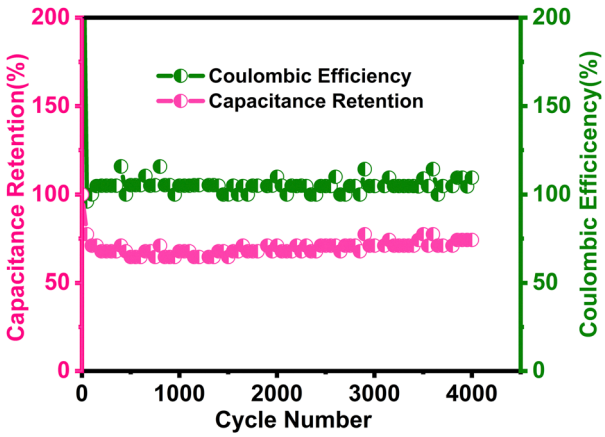

Fig. 11 Long term cyclic stability performance as capacitive retention and Coulombic efficiency of the δ-MnO_2/(3%) Fe_3O_4 nanocomposite sample at 6 A g^{-1} current density over 4000 cycles of operation.

Table 2 Comparison of capacitance of reported MnO_2 based supercapacitors

Electrode	Electrolyte	Specific capacitance (F g^{-1})	Ref.
Fe_3O_4/MnO_2/RGOs	1 M Na_2SO_4	77.5 F g^{-1} at 0.5 A g^{-1}	110
Core–Shell Fe_3O_4 @C@MnO_2	1 M Na_2SO_4	158 F g^{-1} at 0.5 A g^{-1}	111
CoMCNFs@MnO_2	1 M Na_2SO_4	265 F g^{-1} at 0.5 A g^{-1}	112
MnO_2/MXene (nanosheets)	1 M Na_2SO_4	340 F g^{-1} at 1 A g^{-1}	113
rGO/CNT/MnO_2	1 M Na_2SO_4	319 F g^{-1} at 0.5 A g^{-1}	114
MnO_2 nanospheres/carbon nanoparticles/graphene	1 M Na_2SO_4	255 F g^{-1} at 0.5 A g^{-1}	115
MnO_2/PPy/rGO	1 M Na_2SO_4	404 F g^{-1} at 0.25 A g^{-1}	116
CNFs/MnO_2	0.5 M Na_2SO_4	365 F g^{-1} at 1 A g^{-1}	117
δ-MnO_2/(3%) Fe_3O_4	0.5 M Na_2SO_4	459 F g^{-1} at 0.3 A g^{-1}	This work

formation of more nano-porous surface features. This provides more active sites for electrochemical reactions, thus enhancing the capacitance retention by improving the utilization of the electrode material. Oxygen vacancies in MnO_2 also create localized states in the band gap, which could enhance electronic conductivity.[105] These anionic vacancies could also facilitate the ionic transportation phenomenon which is essential for high-rate performance in supercapacitors. Additionally, the presence of oxygen vacancies can enhance redox reactions by providing additional sites for ion insertion and extraction. This improves overall electrochemical performance and contributes to better capacitance retention.[105,106]

During cycling, electrochemical reactions involving intercalations and surface redox processes can perforate the material's surface, thereby exposing new active sites to the electrolyte. Particularly, when electrolyte ions like Na^+ and SO_4^{2-}intercalate the surface of the δ-MnO_2/(3%) Fe_3O_4 nanopetals and engage in surface redox reactions, they abrade this surface. This abrasion can expose additional material from the interior, thereby increasing the reaction site and thus the reaction rate. This can potentially reduce the internal resistance of the electrode, enhancing the electrical conductivity and enable greater charge conduction at the electrode–electrolyte interface.[107] Apart from the electrochemical activation of new active materials, a reduction in agglomeration during cycling along with electrode–electrolyte interface modification could also contribute to the decrement in internal resistance.[108,109] In Fig. 11, initially, the coulombic efficiency was around 96%, which increased to 113% after 4000 cycles, indicating the superior stability of the δ-MnO_2/(3%) Fe_3O_4 composite. Therefore, the observed cycling stability and high efficiency together may have arisen from sustained structural integrity of the electrode, enhanced ionic diffusion within the pores, and improved material wettability over time.[101,102] Overall, the nanocomposite demonstrates favorable morphological and structural characteristics, contributing to its electrochemical stability as observed from the analyses.

Fig. SF3 (ESI†) shows the Comparison between the previously reported MnO_2/Fe_3O_4 based works and our work. Here, it clearly shows that most of the MnO_2/Fe_3O_4 based composite electrode materials at high current densities of 5–6 A g^{-1} exhibit either similar or lower % capacity retention after 4000 cycles than ours. Therefore, in terms of cyclic stability, δ-MnO_2/(3%) Fe_3O_4 exhibits a reasonably good value when compared with other recently published works.

Now Table 2 presents some statistical data for various δ-MnO_2-based electrodes with different morphological and structural characteristics. Among these materials, the δ-MnO_2/(3%) Fe_3O_4 nanocomposite prepared in this study, with 3% diamond-shaped Fe_3O_4 nanoparticles incorporated in δ-MnO_2 nanoflowers, shows the highest specific capacitance. This indicates superior capacitive performance, suggesting that the δ-MnO_2/(3%)Fe_3O_4 nanocomposite electrode can be used in high-performance supercapacitors.

Conclusion

This study investigated the effects of compositing δ-MnO_2 nanoflowers with diamond shaped Fe_3O_4 nanoparticles on electrochemical performances and optimized the combination of the two nanomaterials that would exhibit the best performance. Here, all samples were synthesized *via* a facile hydrothermal route. The diffraction analysis indicated successful synthesis of the desired nanoparticles, with clear differences in lattice parameters of pristine δ-MnO_2 and δ-MnO_2/Fe_3O_4 nanocomposites. Introducing Fe_3O_4 nanodiamonds into pure δ-MnO_2 nanoflowers resulted in reduced crystallinity of the nanocomposites. SEM micrographs also exhibited distinct morphological characteristics arising from incorporation of Fe_3O_4 nanodiamonds into pristine δ-MnO_2 nanoflowers. The *d*-spacing as well as the effective surface area of the pure δ-MnO_2 increased with incorporation of Fe_3O_4 nanodiamonds. However, all the morphological, compositional and structural characterization data exhibited the potential for MnO_2/(3%)Fe_3O_4 nanocomposite to show superior electrochemical performance among all the prepared samples. In the three-electrode system, MnO_2/(3%)Fe_3O_4 nanocomposite electrode exhibited the highest specific capacitance of 459 F g^{-1} at 0.3 A g^{-1} together with excellent cyclic stability with a capacitive retention of 75% after 4000 cycles of operation. Thus, the incorporation of Fe_3O_4 nanodiamonds enhanced the electrochemical performance of δ-MnO_2 nanoflowers. The defect rich structure resulting from the introduction of Fe_3O_4 nanodiamonds into pure δ-MnO_2 gave rise to additional active sites in the material, allowing more electrolyte ions to utilize the outer surface and deeper pores. Moreover, the increase in interlayer spacing also opened up regions within the material to be penetrated by the ions. Hence, the structural and morphological modifications enhanced the interaction between the

electrode and the electrolyte possibly enhancing the underpotential deposition, intercalation and surface redox reactions that are responsible for the improved pseudocapacitive behavior of the δ-MnO_2/Fe_3O_4 nanocomposite. Nonetheless, the performance enhancement peaked at 3 wt% Fe_3O_4 nanodiamond content, beyond which, the excess Fe_3O_4 nanodiamonds started protruding the surface of δ-MnO_2 nanoflowers, prohibiting substantial growth of nano-petals in those regions adversely affecting surface area and interlayer spacing. As a result, the MnO_2/(3%) Fe_3O_4 nanocomposite came out to be the optimized combination exhibiting superior performance than many other similar nanocomposites mentioned in the literature in terms of specific capacitance, which makes it a suitable candidate for high performance supercapacitor application.

Author contributions

Md. Raihan Siddiki: conceptualization, methodology, investigation, formal analysis, writing – original draft. Shahid Abubakar Abtahee: conceptualization, methodology, investigation, formal analysis, writing – original draft. Mizanur Rahaman: investigation, formal analysis. Muhammad Rakibul Islam: investigation, formal analysis. Md. Abdullah Zubair: supervision, conceptualization, methodology, investigation. Writing – review & editing.

Data availability

All necessary data are available within this article.

Conflicts of interest

There are no conflicts to declare.

Acknowledgements

The authors convey their gratitude to the Department of Nanomaterials and Ceramic Engineering and the Department of Physics, BUET, for their support in synthesis and characterization of the materials. We also acknowledge the Committee for Advanced Studies and Research (CASR), BUET, for financial support.

References

1 C. An, Y. Zhang, H. Guo and Y. Wang, *Nanoscale Adv.*, 2019, **1**, 4644–4658.
2 G. Yu, L. Hu, N. Liu, H. Wang, M. Vosgueritchian, Y. Yang, Y. Cui and Z. Bao, *Nano Lett.*, 2011, **11**, 4438–4442.
3 Q. Lu, J. G. Chen and J. Q. Xiao, *Angew. Chem., Int. Ed.*, 2013, **52**, 1882–1889.
4 Z. Yu, L. Tetard, L. Zhai and J. Thomas, *Energy Environ. Sci.*, 2015, **8**, 702–730.
5 X. Lu, C. Wang, F. Favier and N. Pinna, *Adv. Energy Mater.*, 2017, **7**, 1601301.
6 Y. Xu, X. Wang, C. An, Y. Wang, L. Jiao and H. Yuan, *J. Mater. Chem. A*, 2014, **2**, 16480–16488.
7 H. Gao, Y. Li, H. Zhao, J. Xiang and Y. Cao, *Electrochim. Acta*, 2018, **262**, 241–251.
8 S. Raj, P. Kar and P. Roy, *Chem. Commun.*, 2018, **54**, 12400–12403.
9 C. An, Y. Wang, Y. Huang, Y. Xu, L. Jiao and H. Yuan, *Nano Energy*, 2014, **10**, 125–134.
10 G. Wang, L. Zhang and J. Zhang, *Chem. Soc. Rev.*, 2012, **41**, 797–828.
11 S. Chen, M. Xue, Y. Li, Y. Pan, L. Zhu and S. Qiu, *J. Mater. Chem. A*, 2015, **3**, 20145–20152.
12 F. Wang, X. Wu, X. Yuan, Z. Liu, Y. Zhang, L. Fu, Y. Zhu, Q. Zhou, Y. Wu and W. Huang, *Chem. Soc. Rev.*, 2017, **46**, 6816–6854.
13 R. R. Salunkhe, Y. V. Kaneti and Y. Yamauchi, *ACS Nano*, 2017, **11**, 5293–5308.
14 L. Zhang, D. Shi, T. Liu, M. Jaroniec and J. Yu, *Mater. Today*, 2019, **25**, 35–65.
15 Y. Dong, Y. Wang, Y. Xu, C. Chen, Y. Wang, L. Jiao and H. Yuan, *Electrochim. Acta*, 2017, **225**, 39–46.
16 X. Xiao, G. Zhang, Y. Xu, H. Zhang, X. Guo, Y. Liu and H. Pang, *J. Mater. Chem. A*, 2019, **7**, 17266–17271.
17 X. Guo, Y.-Z. Zhang, F. Zhang, Q. Li, D. H. Anjum, H. Liang, Y. Liu, C. Liu, H. N. Alshareef and H. Pang, *J. Mater. Chem. A*, 2019, **7**, 15969–15974.
18 J. Ma, X. Guo, Y. Yan, H. Xue and H. Pang, *Adv. Sci.*, 2018, **5**, 1700986.
19 X. Li, J. Wei, Q. Li, S. Zheng, Y. Xu, P. Du, C. Chen, J. Zhao, H. Xue, Q. Xu and H. Pang, *Adv. Funct. Mater.*, 2018, **28**, 1800886.
20 H.-S. Kim, J. B. Cook, H. Lin, J. S. Ko, S. H. Tolbert, V. Ozolins and B. Dunn, *Nat. Mater.*, 2017, **16**, 454–460.
21 I. Rabani, A. Younus, S. Patil and Y.-S. Seo, *Dalton Trans.*, 2022, **51**, 14190–14200.
22 A. Allagui, A. S. Elwakil, M. E. Fouda and A. G. Radwan, *J. Power Sources*, 2018, **390**, 142–147.
23 F. Hekmat, S. Shahrokhian and N. Taghavinia, *J. Phys. Chem. C*, 2018, **122**, 27156–27168.
24 Z. Ma, F. Jing, Y. Fan, L. Hou, L. Su, L. Fan and G. Shao, *Small*, 2019, **15**, 1900862.
25 J. Shin, D. Shin, H. Hwang, T. Yeo, S. Park and W. Choi, *J. Mater. Chem. A*, 2017, **5**, 13488–13498.
26 A. Zhang, R. Zhao, L. Hu, R. Yang, S. Yao, S. Wang, Z. Yang and Y. Yan, *Adv. Energy Mater.*, 2021, **11**, 2101412.
27 Y.-P. Zhu, C. Xia, Y. Lei, N. Singh, U. Schwingenschlögl and H. N. Alshareef, *Nano Energy*, 2019, **56**, 357–364.
28 W. Li, J. Shao, Q. Liu, X. Liu, X. Zhou and J. Hu, *Electrochim. Acta*, 2015, **157**, 108–114.
29 W. Lu, Y. Li, M. Yang, X. Jiang, Y. Zhang and Y. Xing, *ACS Appl. Energy Mater.*, 2020, **3**, 8190–8197.
30 K. T. Kubra, R. Sharif, B. Patil, A. Javaid, S. Shahzadi, A. Salman, S. Siddique and G. Ali, *J. Alloys Compd.*, 2020, **815**, 152104.
31 Z. Luan, Y. Tian, L. Gai, H. Jiang, X. Guo and Y. Yang, *J. Alloys Compd.*, 2017, **729**, 9–18.

32 B. L. Vijayan, S. G. Krishnan, N. K. M. Zain, M. Harilal, A. Yar, I. I. Misnon, J. O. Dennis, M. M. Yusoff and R. Jose, *Chem. Eng. J.*, 2017, **327**, 962–972.
33 R. B. Pujari, S. J. Patil, J. Park, A. Shanmugasundaram and D.-W. Lee, *J. Power Sources*, 2019, **436**, 226826.
34 A. J. C. Mary, S. S. Shalini, R. Balamurugan, M. P. Harikrishnan and A. C. Bose, *New J. Chem.*, 2020, **44**, 11316–11323.
35 C. Zhang, Z. Peng, Y. Chen, H. Chen, B. Zhang, H. Cheng, J. Wang and M. Deng, *Electrochim. Acta*, 2020, **347**, 136246.
36 J. Tang, M. Myers, K. A. Bosnick and L. E. Brus, *J. Phys. Chem. B*, 2003, **107**, 7501–7506.
37 X. Xue, P. Deng, B. He, Y. Nie, L. Xing, Y. Zhang and Z. L. Wang, *Adv. Energy Mater.*, 2014, **4**, 1301329.
38 C. Tu, X. Li, C. Lu, Q. Luo, T. Li and M. Zhu, *Mater. Chem. Front.*, 2022, **6**, 1938–1947.
39 Y. Liu, P. Li, Y. Wang, J. Liu, Y. Wang, J. Zhang, M. Wu and J. Qiu, *J. Alloys Compd.*, 2017, **695**, 2612–2618.
40 X. Wang, D. Jiang, C. Jing, X. Liu, K. Li, M. Yu, S. Qi and Y. Zhang, *J. Energy Storage*, 2020, **30**, 101554.
41 E. Payami and R. Teimuri-Mofrad, *Electrochim. Acta*, 2021, **383**, 138296.
42 N. Wang, G. Ding, X. Yang, L. Zhao and D. He, *Mater. Lett.*, 2019, **255**, 126589.
43 Y. Wang, S. Rao, P. Mao, F. Zhang, P. Xiao, L. Peng and Q. Zhu, *Electrochim. Acta*, 2020, **337**, 135739.
44 C. Zeng, W. Weng, T. Lv and W. Xiao, *ACS Appl. Mater. Interfaces*, 2018, **10**, 30470–30478.
45 J. Zhu, S. Tang, H. Xie, Y. Dai and X. Meng, *ACS Appl. Mater. Interfaces*, 2014, **6**, 17637–17646.
46 D. Sarkar, G. G. Khan, A. K. Singh and K. Mandal, *J. Phys. Chem. C*, 2013, **117**, 15523–15531.
47 Q. Chen, W. Wei, J. Tang, J. Lin, S. Li and M. Zhu, *Electrochim. Acta*, 2019, **317**, 628–637.
48 N. Torres-Gómez, O. Nava, L. Argueta-Figueroa, R. García-Contreras, A. Baeza-Barrera and A. R. Vilchis-Nestor, *J. Nanomater.*, 2019, **2019**, 1–15.
49 B.-H. Park and J.-H. Choi, *Electrochim. Acta*, 2010, **55**, 2888–2893.
50 H.-K. Park, B.-S. Kong and E.-S. Oh, *Electrochem. Commun.*, 2011, **13**, 1051–1053.
51 J. M. D. O. Cremonezzi, D. Y. Tiba and S. H. Domingues, *SN Appl. Sci.*, 2020, **2**, 1689.
52 O. Ghodbane, J.-L. Pascal and F. Favier, *ACS Appl. Mater. Interfaces*, 2009, **1**, 1130–1139.
53 X.-L. Li and Y.-D. Li, *J. Phys. Chem. B*, 2004, **108**, 13893–13900.
54 G. Du, Z. Guo, S. Wang, R. Zeng, Z. Chen and H. Liu, *Chem. Commun.*, 2010, **46**, 1106–1108.
55 H. Li, K. Yu, X. Lei, B. Guo, H. Fu and Z. Zhu, *J. Phys. Chem. C*, 2015, **119**, 22681–22689.
56 M. A. Zubair, T. K. Mouri and M. T. Chowdhury, *Phys. Chem. Chem. Phys.*, 2023, **25**, 27628–27653.
57 L. Yan, C. Shen, L. Niu, M. Liu, J. Lin, T. Chen, Y. Gong, C. Li, X. Liu and S. Xu, *ChemSusChem*, 2019, **12**, 3571–3581.
58 V. Radmilovic, H. A. Gasteiger and P. N. Ross, *J. Catal.*, 1995, **154**, 98–106.
59 K. K. Paul, N. Sreekanth, R. K. Biroju, T. N. Narayanan and P. K. Giri, *Sol. Energy Mater. Sol. Cells*, 2018, **185**, 364–374.
60 L. Ma, L. Xu, X. Xu, X. Zhou, J. Luo and L. Zhang, *Mater. Sci. Eng., B*, 2016, **212**, 30–38.
61 G. Tang, Y. Wang, W. Chen, H. Tang and C. Li, *Mater. Lett.*, 2013, **100**, 15–18.
62 R. Zhou, C. Han and X. Wang, *J. Power Sources*, 2017, **352**, 99–110.
63 X. Li, L. Zhang, X. Zang, X. Li and H. Zhu, *ACS Appl. Mater. Interfaces*, 2016, **8**, 10866–10873.
64 A. Gigot, M. Fontana, M. Serrapede, M. Castellino, S. Bianco, M. Armandi, B. Bonelli, C. F. Pirri, E. Tresso and P. Rivolo, *ACS Appl. Mater. Interfaces*, 2016, **8**, 32842–32852.
65 A. M. Alsaad, A. A. Ahmad, Q. M. Al-Bataineh, A. A. Bani-Salameh, H. S. Abdullah, I. A. Qattan, Z. M. Albataineh and A. D. Telfah, *Materials*, 2020, **13**, 1737.
66 M. Fang, G. Dong, R. Wei and J. C. Ho, *Adv. Energy Mater.*, 2017, **7**, 1700559.
67 X. Liang, J. E. Post, B. Lanson, X. Wang, M. Zhu, F. Liu, W. Tan, X. Feng, G. Zhu and X. Zhang, *Environ. Sci.: Nano*, 2020, **7**, 238–249.
68 S. Agarwala, Z. H. Lim, E. Nicholson and G. W. Ho, *Nanoscale*, 2012, **4**, 194–205.
69 B. B. Li, S. Z. Qiao, X. R. Zheng, X. J. Yang, Z. D. Cui, S. L. Zhu, Z. Y. Li and Y. Q. Liang, *J. Power Sources*, 2015, **284**, 68–76.
70 D. Wang, Z. Pan, Z. Wu, Z. Wang and Z. Liu, *J. Power Sources*, 2014, **264**, 229–234.
71 L. Wang, X. Tan, Q. Zhu, Z. Dong, X. Wu, K. Huang and J. Xu, *J. Power Sources*, 2022, **518**, 230747.
72 X. Mao, Y. Zou, F. Xu, L. Sun, H. Chu, H. Zhang, J. Zhang and C. Xiang, *ACS Appl. Mater. Interfaces*, 2021, **13**, 22664–22675.
73 R. Zhou, S. Wei, Y. Liu, N. Gao, G. Wang, J. Lian and Q. Jiang, *Sci. Rep.*, 2019, **9**, 3980.
74 G. K. Sharma, B. Ranjan and D. Kaur, *Appl. Phys. Lett.*, 2021, **118**, 203901.
75 M. R. Siddiki, S. A. Abtahee and M. A. Zubair, in *Comprehensive Materials Processing*, ed. S. Hashmi, Elsevier, Oxford, 2nd edn, 2024, pp. 340–379.
76 T. Xiong, W. S. V. Lee and J. Xue, *ACS Appl. Energy Mater.*, 2018, acsaem.8b01160.
77 B. A. Ali, O. I. Metwalli, A. S. G. Khalil and N. K. Allam, *ACS Omega*, 2018, **3**, 16301–16308.
78 S.-L. Kuo, J.-F. Lee and N.-L. Wu, *J. Electrochem. Soc.*, 2006, **154**, A34.
79 S. K. Ghosh, *ACS Omega*, 2020, **5**, 25493–25504.
80 Y. Liu, S. P. Jiang and Z. Shao, *Mater. Today Adv.*, 2020, **7**, 100072.
81 Y. Wang, Z. Shi, Y. Huang, Y. Ma, C. Wang, M. Chen and Y. Chen, *J. Phys. Chem. C*, 2009, **113**, 13103–13107.
82 M. Toupin, T. Brousse and D. Bélanger, *Chem. Mater.*, 2002, **14**, 3946–3952.
83 X.-L. Bai, Y.-L. Gao, Z.-Y. Gao, J.-Y. Ma, X.-L. Tong, H.-B. Sun and J. A. Wang, *Appl. Phys. Lett.*, 2020, **117**, 183901.

84 M. H. Ahmad, R. B. Alam, A. Ul-Hamid, S. F. U. Farhad and M. R. Islam, *J. Energy Storage*, 2022, **47**, 103551.
85 Y. Chen, W. Ma, K. Cai, X. Yang and C. Huang, *Electrochim. Acta*, 2017, **246**, 615–624.
86 A. K. Thakur, A. B. Deshmukh, R. B. Choudhary, I. Karbhal, M. Majumder and M. V. Shelke, *Mater. Sci. Eng., B*, 2017, **223**, 24–34.
87 S. Zhu, L. Li, J. Liu, H. Wang, T. Wang, Y. Zhang, L. Zhang, R. S. Ruoff and F. Dong, *ACS Nano*, 2018, **12**, 1033–1042.
88 S. Guo, W. Chen, M. Li, J. Wang, F. Liu and J. P. Cheng, *Electrochim. Acta*, 2018, **271**, 498–506.
89 J.-H. Lin, *Materials*, 2018, **11**, 263.
90 S. S. Nardekar, K. Krishnamoorthy, P. Pazhamalai, S. Sahoo, V. K. Mariappan and S.-J. Kim, *J. Mater. Chem. A*, 2020, **8**, 13121–13131.
91 M. A. A. Mohd Abdah, N. A. Zubair, N. H. N. Azman and Y. Sulaiman, *Mater. Chem. Phys.*, 2017, **192**, 161–169.
92 M. Gaire, K. Liang, S. Luo, B. Subedi, S. Adireddy, K. Schroder, S. Farnsworth and D. B. Chrisey, *RSC Adv.*, 2020, **10**, 16817–16825.
93 W. Cai, T. Lai, W. Dai and J. Ye, *J. Power Sources*, 2014, **255**, 170–178.
94 Y. Liu, D. He, H. Wu, J. Duan and Y. Zhang, *Electrochim. Acta*, 2015, **164**, 154–162.
95 P. Si, S. Ding, X.-W. (David) Lou and D.-H. Kim, *RSC Adv.*, 2011, **1**, 1271.
96 Y. A. Tarek, R. Shakil, A. H. Reaz, C. K. Roy, H. R. Barai and S. H. Firoz, *ACS Omega*, 2022, **7**, 20145–20154.
97 K. O. Oyedotun, A. A. Mirghni, O. Fasakin, D. J. Tarimo, B. A. Mahmoud and N. Manyala, *J. Energy Storage*, 2021, **36**, 102419.
98 C. Zhao, X. Shao, Y. Zhang and X. Qian, *ACS Appl. Mater. Interfaces*, 2016, **8**, 30133–30142.
99 R. Ren, M. S. Faber, R. Dziedzic, Z. Wen, S. Jin, S. Mao and J. Chen, *Nanotechnology*, 2015, **26**, 494001.
100 Z. Gao, J. Wang, Z. Li, W. Yang, B. Wang, M. Hou, Y. He, Q. Liu, T. Mann, P. Yang, M. Zhang and L. Liu, *Chem. Mater.*, 2011, **23**, 3509–3516.
101 Z. Ling, Z. Wang, M. Zhang, C. Yu, G. Wang, Y. Dong, S. Liu, Y. Wang and J. Qiu, *Adv. Funct. Mater.*, 2016, **26**, 111–119.
102 K. Xu, S. Li, J. Yang, H. Xu and J. Hu, *J. Alloys Compd.*, 2016, **678**, 120–125.
103 W. Chen, R. B. Rakhi, Q. Wang, M. N. Hedhili and H. N. Alshareef, *Adv. Funct. Mater.*, 2014, **24**, 3130–3143.
104 J. Shao, X. Zhou, Q. Liu, R. Zou, W. Li, J. Yang and J. Hu, *J. Mater. Chem. A*, 2015, **3**, 6168–6176.
105 T. Zhai, S. Xie, M. Yu, P. Fang, C. Liang, X. Lu and Y. Tong, *Nano Energy*, 2014, **8**, 255–263.
106 L. Zhao, W. Wang, H. Zhao, M. Wang, B. Ge, X. Shao and W. Li, *Appl. Surf. Sci.*, 2019, **491**, 24–31.
107 M. R. Islam, S. N. S. Pias, R. B. Alam and S. I. Khondaker, *Nano Express*, 2020, **1**, 030013.
108 M. R. Islam and S. I. Mollik, *Heliyon*.
109 D. Li, W. Zhou, Q. Zhou, G. Ye, T. Wang, J. Wu, Y. Chang and J. Xu, *Nanotechnology*, 2017, **28**, 395401.
110 J. Li, Y. Chen, Q. Wu and H. Xu, *J. Alloys Compd.*, 2017, **693**, 373–380.
111 Z. Li, Y. Yao, Y. Zheng, T. Gao, Z. Liu and G. Zhou, *J. Electrochem. Soc.*, 2018, **165**, E58.
112 X. Sun, T. Xu, J. Bai and C. Li, *ACS Appl. Energy Mater.*, 2019, **2**, 8675–8684.
113 S. Chen, Y. Xiang, W. Xu and C. Peng, *Inorg. Chem. Front.*, 2019, **6**, 199–208.
114 H. Jiang, Y. Dai, Y. Hu, W. Chen and C. Li, *ACS Sustainable Chem. Eng.*, 2014, **2**, 70–74.
115 Y. Xiong, M. Zhou, H. Chen, L. Feng, Z. Wang, X. Yan and S. Guan, *Appl. Surf. Sci.*, 2015, **357**, 1024–1030.
116 G. Han, Y. Liu, E. Kan, J. Tang, L. Zhang, H. Wang and W. Tang, *RSC Adv.*, 2014, **4**, 9898–9904.
117 J.-G. Wang, Y. Yang, Z.-H. Huang and F. Kang, *J. Power Sources*, 2013, **224**, 86–92.